applied sciences

Article

Application of a Novel Weighted Essentially Non-Oscillatory Scheme for Reynolds-Averaged Stress Model and Reynolds-Averaged Stress Model/Large Eddy Simulation (RANS/LES) Coupled Simulations in Turbomachinery Flows

Hao Wang, Dongdong Zhong, Shuo Zhang, Xingshuang Wu and Ning Ge *

College of Energy and Power Engineering, Nanjing University of Aeronautics and Astronautics, Nanjing 210016, China; hwangnd@nuaa.edu.cn (H.W.); zhong901222@163.com (D.Z.); shuozhang0715@nuaa.edu.cn (S.Z.); wxsnuaa@nuaa.edu.cn (X.W.)

* Correspondence: gening@nuaa.edu.cn

Featured Application: This study demonstrates the application of high-order WENO-ZQ schemes in aerodynamic simulations of aircraft engine components. By integrating WENO-ZQ into NUAA-Turbo2.0 and employing RANS and hybrid RANS/LES turbulence models, we conducted detailed computations and simulations of aircraft engine compressors, high-pressure turbines, and turbine film cooling. Using WENO-ZQ enhances simulation accuracy and efficiency, effectively capturing critical flow details such as turbine wakes and film cooling distribution. This work highlights the importance of advanced numerical schemes in guiding the design and analysis of modern turbomachinery.

Abstract: In numerical simulations, achieving high accuracy without significantly increasing computational cost is often a challenge. To address this issue, this paper proposes an improved finite volume Weighted Essentially Non-Oscillatory (WENO) scheme for structured grids. By employing a single-point quadrature rule to perform flux integration on the control volume faces, this scheme is designed for use in NUAA-Turbo three-dimensional fluid solvers based on structured grids, utilizing RANS and RANS/LES coupling to simulate turbomachinery flows. Firstly, the new WENO scheme is validated against classical numerical test cases to evaluate its stability and reliability in handling discontinuities, double Mach reflection problems, and Rayleigh–Taylor (RT) instability. Compared to the original scheme, this improved finite-volume WENO scheme demonstrates better stability near discontinuities and more effectively resolves flow features at the same grid resolution. Next, for engineering applications related to turbomachinery, such as compressor and turbine characteristics, calculations using RANS are performed and the results obtained with WENO-ZQ3 and WENO-JS3 are compared. Finally, the new fifth-order WENO scheme is applied to RANS/LES coupling simulations of turbine wake and film cooling. The results indicate that the improved finite-volume WENO scheme provides better stability and accuracy in engineering applications. For instance, the average error in calculating compressor efficiency characteristics is reduced from 0.76% to 0.05%, the error in turbine vane pressure distribution compared to the experimental values is within 1%, and the error in film cooling efficiency centerline distribution compared to the experimental values is within 3%. Additionally, the qualitative results of turbine wake and film cooling show that even with a small number of grid points, more detailed flow physics can be captured, thereby reducing computational costs in aerodynamic applications.

Keywords: WENO scheme; turbomachinery flow; NUAA-Turbo; RANS; RANS/LES coupled simulations

check for updates

Citation: Wang, H.; Zhong, D.; Zhang, S.; Wu, X.; Ge, N. Application of a Novel Weighted Essentially Non-Oscillatory Scheme for Reynolds-Averaged Stress Model and Reynolds-Averaged Stress Model/Large Eddy Simulation (RANS/LES) Coupled Simulations in Turbomachinery Flows. *Appl. Sci.* **2024**, *14*, 5085. https://doi.org/10.3390/app14125085

Academic Editor: Francesca Scargiali

Received: 27 April 2024
Revised: 31 May 2024
Accepted: 5 June 2024
Published: 11 June 2024

1. Introduction

With the development of science and technology, scholars are paying more and more attention to the flow mechanism. Numerical simulation can shorten the research cycle and save costs, which is one of the important ways to conduct flow mechanism research. For simulation methods such as large eddy simulation (LES) and direct numerical simulation (DNS), a large number of grids and longer computation time are often required to obtain very detailed calculation results, which goes against the advantages of numerical simulation. Therefore, high-order schemes have been studied and combined with a series of numerical simulation methods, enabling numerical simulations to capture more detailed physical details with fewer grids [1,2].

In the process of solving the Navier–Stokes equations, scholars have observed that the solutions of the nonlinear equations exhibit discontinuities, regardless of the smoothness of the initial conditions. To address this issue, researchers have attempted to improve Weighted Essentially Non-Oscillatory (WENO) schemes, and it has been found that this approach can make numerical solving methods more efficient and accurate [3].

An essentially non-oscillatory (ENO) scheme was proposed in 1987, which achieved high-order accuracy and avoided oscillations in the solution. However, it was soon found to be unstable under certain unfavorable initial conditions [4]. Therefore, in the 1990s, the ENO scheme was improved and developed into the WENO scheme by Liu et al. [5]. Subsequently, Jiang and Shu [6] further improved the WENO scheme and proposed a general framework for the design of smoothness indicators and nonlinear weights by averaging k stencils to achieve a $2k-1$ order of accuracy in smooth regions while maintaining a k order of accuracy at discontinuities. This led to the classical WENO schemes [7–9].

Although the classical WENO schemes have many advantages, they exhibit several drawbacks in engineering applications [10]:

1. The computational cost is very high, and the calculation process is complex.
2. The optimal (linear) weights depend on the geometry of the mesh and may become negative in some cases, meaning they lack robustness.
3. The drawbacks become more pronounced with an increase in spatial dimension.

To enhance the engineering application value of the WENO scheme, Zhu and Qiu [11] developed a new fifth-order finite-difference WENO-ZQ scheme in 2016, which was later extended to a finite-volume version in multiple dimensions [12]. This new class of WENO schemes uses a convex combination of a quartic polynomial with two linear polynomials on unequal-sized spatial stencils in one dimension and is extended to two dimensions in a dimension-by-dimension fashion. It is more efficient, simpler, and easily extendable to multiple dimensions. The associated linear weights are artificially set to be any random positive numbers, with the only requirement being that their sum equals one. This property ensures that the optimal (linear) weights do not depend on the geometry of the mesh, and the problem of negative linear weights observed in classical WENO-JS schemes [8] is mitigated.

Additionally, in the context of solving steady-state problems using classical WENO schemes [6,7], it is common for the residual to plateau at a level above machine zero, equivalent to the truncation error. This occurs even when there is minimal observable change in the physical variables over successive time iterations [13]. Numerous scholars have explored various methods to mitigate this issue. However, research indicates [13] that WENO-ZQ can converge to machine zero without requiring any modifications across a range of standard test cases. These encompass scenarios with strong shocks, contact discontinuities, rarefaction waves, and their interactions, and intricate wave dynamics interacting with computational boundaries.

In recent years, numerous scholars have improved WENO-ZQ and applied it in various engineering applications. Zhong and Sheng [2,14–16] extended the WENO-ZQ scheme by introducing the concept of phantom points and applied it to predict transitional and separated flows with RANS modeling. Dinshaw S. Balsara et al. [4,17] adopted the idea of WENO-ZQ, replacing two small second-order stencils with three third-order stencils, and developed WENO-AO. Zhao et al. [18] proposed a new fifth-order hybrid WENO scheme by integrating methods from [19]. The major advantage of this scheme is its higher efficiency with fewer numerical errors in smooth regions and lower computational costs. Lin et al. [20] proposed a high-order residual distribution conservative finite-difference WENO-ZQ scheme for solving steady-state hyperbolic equations with source terms on uniform meshes. They applied this method to both scalar and system test problems, including Burgers' equation, shallow water equations, nozzle flow problems, Cauchy–Riemann problems, and Euler equations.

In addition to the WENO scheme, recent scholars have proposed the high-order TENO (Targeted Essentially Non-Oscillatory) scheme, which boasts high-order accuracy, low numerical dissipation, and sharp shock-capturing capabilities. Zhe Ji et al. [21] extended this high-order shock-capturing TENO scheme from being applicable only to Cartesian or curvilinear coordinate grids to being applicable to unstructured grids. By employing a reconstruction strategy with large and small stencils, the TENO scheme achieves excellent numerical stability. Francesco De Vanna et al. [22] used both WENO and TENO schemes in a GPU-accelerated compressible flow solver to solve two-dimensional Riemann problems, yielding good results.

Despite the promising results and significant potential for the development of the TENO scheme, the WENO scheme is currently more widely used and has been more extensively developed, making it better suited for broader application in engineering examples. Over the past few years, research on the improved WENO-ZQ scheme has become relatively mature, but there are no reported applications of the finite-volume version of the WENO-ZQ scheme in solving engineering problems. Therefore, this paper derives the applicability of this scheme by implementing flux integration on control volume faces using a single-point quadrature rule, making the scheme more suitable for structured grids. The improved scheme is embedded into the NUAA-Turbo2.0 three-dimensional compressible solver based on structured grids. Using turbulence models such as RANS and hybrid RANS/LES models (SST-SAS), calculations and simulations are conducted for aircraft engine compressors, high-pressure turbines, and turbine film cooling to demonstrate the scheme's applicability in engineering. This also involves physical phenomena such as turbine wake and film cooling efficiency distribution.

This paper first briefly explains the one-dimensional finite-volume WENO-ZQ and compares it with WENO-JS. Then, several classic schemes are compared by solving Riemann problems, double Mach reflection problems, and Rayleigh–Taylor (RT) instability problems. Finally, high-fidelity predictions are made by solving engineering applications related to compressor and turbine characteristics, as well as turbine flow field simulations focusing on wake and film cooling issues. The third-order and fifth-order finite-volume versions of the WENO-ZQ scheme are systematically tested on structured grids.

2. WENO-ZQ Schemes

Before applying the finite-volume form of the WENO-ZQ scheme, let us first provide a brief introduction. Consider the one-dimensional hyperbolic conservation law

$$\begin{cases} u_t + f(u)_x = 0, \\ u(x,0) = u_0(x), \end{cases} \tag{1}$$

which is discretized in the computational domain using a uniform cell size h. Integrating Equation (1) in a control volume $I_i = [x_{i-1/2}, x_{i+1/2}]$ cell yields

$$\frac{d\overline{u}(x_i,t)}{dt} + \frac{1}{h}[f(u(x_{i+1/2},t)) - f(u(x_{i-1/2},t))] = 0, \tag{2}$$

where $\overline{u}(x_i,t)$ is the average value of u over the cell I_i at time. Equation (2) can be rewritten as

$$\frac{d\overline{u}(x_i,t)}{dt} = L(u_i) = -\frac{1}{h}\left(\hat{f}_{i+1/2} - \hat{f}_{i-1/2}\right).$$

The Roe-difference splitting scheme [23] and AUSM-up flux splitting scheme [24] are employed in this paper to calculate the numerical flux using the equation

$$\begin{cases} ROE: & \hat{f}_{i+1/2} = \frac{1}{2}\left(f\left(u^L\right) + f\left(u^R\right)\right) - \frac{1}{2}\left|\overline{A}\right|\left(u^R - u^L\right), \\ \text{AUSM} - up: & \hat{f}_{i+1/2} = F^{(c)}_{i+1/2} + P_{i+1/2} = m_{i+1/2}\vec{\psi}_{i+1/2} + P_{i+1/2}, \end{cases} \tag{3}$$

where u^L and u^R are the reconstructed left and right valuables on the face of the control volume I_i. The Roe scheme is used in transonic flow, and AUSM-up is used in low-speed flow, supersonic flow, and LES simulation.

Based on this approach [13], a new fifth-order WENO-ZQ scheme (referred to as WENO-ZQ5) was proposed by Zhu and Qiu [11,12]. They innovatively constructed an adaptive formula, enabling the use of a large stencil in smooth regions and two small stencils in capturing discontinuities. This new fifth-order WENO-ZQ scheme features positive linear weights and high accuracy. The procedure of WENO-ZQ5 is summarized as follows:

1. Choose the big central spatial stencil $T_1 = \{I_{i-2}, I_{i-1}, I_i, I_{i+1}, I_{i+2}\}$ and the other two smaller stencils $T_2 = \{I_{i-1}, I_i\}$ and $T_3 = \{I_i, I_{i+1}\}$ to reconstruct the polynomials $p_1(x)$, $p_2(x)$, and $p_3(x)$. Additionally, the generalized expression for the reconstructed polynomial on nonuniform meshes provided by Shu [25] is adopted in this paper.
2. Compute the smoothness indicators $\beta_l, l = 1,2,3$, which are obtained through a multiple of the local grid spacing and the difference in polynomial values at adjacent points:

$$\beta_l = \sum_{k=1}^{r} \int_{I_i} h^{2k-1} \left(\frac{d^k p_l(x)}{dx^k} \right)^2 dx, l = 1,2,3 \tag{4}$$

3. Calculate the nonlinear weights based on the linear weights and the smoothness indicators. An adaptive formula for τ is written based on the difference between β_1, β_2, and β_3 as follows:

$$\tau = \left(\frac{|\beta_1 - \beta_2| + |\beta_1 - \beta_3|}{2} \right)^2$$

The nonlinear weights ω_l, l = 1, 2, 3 in the expression are then expressed as

$$\omega_l = \left(\frac{\overline{\omega}_l}{\overline{\omega}_1 + \overline{\omega}_2 + \overline{\omega}_3} \right), \ \overline{\omega}_l = \gamma_l \left(1 + \frac{\tau}{\beta_l + \varepsilon} \right), \ l = 1,2,3$$

where γ_l represents the positive linear weights, with the only requirement being that $\gamma_1 + \gamma_2 + \gamma_3 = 1$ ($\gamma_1 \neq 0$). Here, ε is a small positive number to avoid the denominator becoming zero.
4. The final reconstruction formulation of conservative values $u(x,\ t)$ at the point $x_{i+1/2}$ of the target cell I_i is given by $\beta_l, l = 1,2,3$.

$$u^L_{i+\frac{1}{2}} = \omega_1 \left(\frac{1}{\gamma_1} p_1(x) - \frac{\gamma_2}{\gamma_1} p_2(x) - \frac{\gamma_3}{\gamma_1} p_3(x) \right) + \omega_2 p_2(x) + \omega_3 p_3(x) \tag{5}$$

The procedure of WENO-JS5 is summarized as follows:

1. Choose the big spatial stencil $T_1 = \{I_{i-2}, I_{i-1}, I_i, I_{i+1}, I_{i+2}\}$ and the other three equidistant stencils $T_1^{\text{js}} = \{I_{i-2}, I_{i-1}, I_i\}$,$T_2^{\text{js}} = \{I_{i-1}, I_i, I_{i+1}\}$, and $T_3^{\text{js}} = \{I_i, I_{i+1}, I_{i+1}\}$ to reconstruct the polynomials p_1, p_1^{js}, p_2^{js} and p_3^{js}.
2. Compute the linear weights based on the polynomials p_1, p_1^{js}, p_2^{js} and p_3^{js} as follows:

$$p_1 = \gamma_1^{js} p_1^{js} + \gamma_2^{js} p_2^{js} + \gamma_3^{js} p_3^{js},$$

$\gamma_l^{js}, l = 1,2,3$ are linear weights in the WENO-JS5 scheme. In a uniform grid, $\gamma_1^{js} = 0.3, \gamma_2^{js} = 0.6,$ and $\gamma_3^{js} = 0.1$.

3. Compute the smoothness indicators $\beta_l, l = 1,2,3$ based on Formula (4):
4. Calculate the nonlinear weights based on the linear weights and the smoothness indicators.

$$\alpha_l = \frac{\gamma_l^{js}}{(\varepsilon + \beta_l)^2}, \overline{\omega}_l^{js} = \frac{\alpha_k}{\sum\limits_{l=0}^{r-1} \alpha_l}, l = 1,2,3$$

5. The final reconstruction formulation of conservative values $u(x,\ t)$ at the point $x_{i+1/2}$ of the target cell I_i is given by

$$u^L_{i+\frac{1}{2}} = \overline{\omega}_1^{js} p_1^{js} + \overline{\omega}_2^{js} p_2^{js} + \overline{\omega}_3^{js} p_3^{js}. \tag{6}$$

In the comparison of the calculation procedures, WENO-ZQ5 does not need to solve the linear weights and does not need to care about the situation of negative linear weights, which increases the robustness of the calculation and reduces the computational cost. Its linear weights are not dependent on a grid and are convenient to apply to non-uniform meshes and adaptive meshes. For the the NUAA-Turbo2.0 three-dimensional compressible solver using WENO-JS5, only appropriate deletion is needed to achieve its application. Although the new scheme proposed by Zhu and Qiu is of fifth-order accuracy, it can be extended to third-order accuracy by only replacing the polynomial and smoothing factor of the third-order big central spatial stencil, which is denoted as WENO-ZQ3.

3. Classic Numerical Scheme Test Cases

3.1. Solving the One-Dimensional Euler Equations under Riemann Initial Conditions

The Riemann problem is a fundamental scenario in computational fluid dynamics, often used to study the behavior of shock waves and discontinuities in fluid flow. It involves solving the Euler equations with piecewise constant initial conditions that include a discontinuity, leading to complex wave interactions within the fluid medium. This problem is crucial for understanding the dynamics of shock waves, rarefaction waves, and contact discontinuities, which are essential for accurately modeling fluid behavior under various conditions.

In the current study, we consider one-dimensional Euler equations with specific initial conditions defined over the domain $x \in [-5, 5]$, as shown in Equation (7). The computational domain is discretized using 200 grid points.

$$\frac{\partial}{\partial t}\begin{pmatrix} \varrho \\ \varrho u \\ E \end{pmatrix} + \frac{\partial}{\partial x}\begin{pmatrix} \varrho u \\ \varrho u^2 + p \\ u(E+p) \end{pmatrix} = 0. \tag{7}$$

The initial conditions for the Riemann problem are given by Equation (8), where T = 1.6. The initial conditions are set to create a discontinuity, which then evolves over time, providing insights into the fluid's response to abrupt changes in pressure, density, and velocity. The study of Riemann problems is pivotal for validating numerical methods and enhancing the accuracy of simulations involving shock waves and other discontinuous phenomena in fluid dynamics.

$$(\varrho, u, p, \gamma)^T = \begin{cases} (0.445, 0.698, 3.528, 1.4)^T, & x \in [-5, 0), \\ (0.5, 0, 0.571, 1.4)^T, & , x \in [0, 5]. \end{cases} \tag{8}$$

In Figure 1, the horizontal axis represents the range of the independent variable, with units in millimeters (mm), while the vertical axis represents the dimensionless density. And the exact solution is represented by a solid line, while solutions from different numerical schemes are denoted by various symbols. It can be observed that the new WENO scheme exhibits advantages in resolving discontinuities, showing better stability and resolution compared to the WENO3-JS format. Additionally, the superiority of the new WENO scheme in terms of stability and resolution at discontinuities becomes even more pronounced when compared to WENO4 and WENO5.

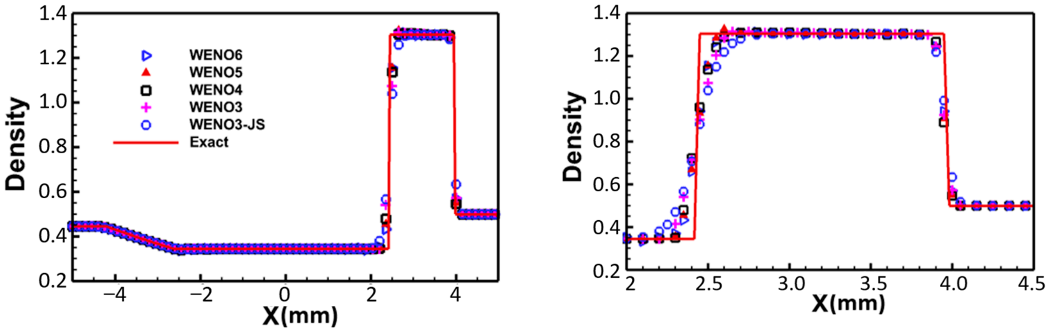

Figure 1. The results of solving the Lax problem using different numerical schemes. (**a**) Full range; (**b**) interrupted position.

3.2. Numerical Simulation of the Double Mach Reflection Problem

The double Mach reflection problem (DMRP) is a classic scenario in compressible fluid dynamics that involves the complex reflection of shock waves propagating within a fluid medium. This phenomenon occurs when a shock wave interacts with a rigid wall, resulting in two distinct Mach reflections within the fluid. The study of DMRP is crucial for understanding shock wave dynamics and fluid behavior under extreme conditions. In our computational study, we consider two-dimensional Euler equations with specific initial conditions defined over a domain of $[0, 4] \times [0, 1]$. The specific initial conditions are as follows:

$$(\varrho, p, u, v, \gamma)^T = \begin{cases} (8, 116.5, 7.14471, \ -4.125, 1.4)^T, & x \geq \sqrt{3}\left(x - \frac{1}{6}\right), \\ (1.4, 1.0, 0, 0, 1.4)^T, & , x < \sqrt{3}\left(x - \frac{1}{6}\right). \end{cases} \tag{9}$$

The boundary conditions are carefully prescribed to capture the reflective and shock wave interactions accurately. At the left boundary $(x = 0)$, we impose inflow conditions to initiate shock wave propagation. The right boundary $(x = 4)$ is set as a reflective boundary to simulate the wall interaction. The bottom boundary $(y = 0)$ presents a unique scenario where an exact solution is provided for $0 \leq x \leq 1/6$. This serves as a reference region for validating the numerical results. For $1/6 \leq x \leq 4$, symmetric boundary conditions are employed to maintain flow symmetry. At the top boundary $(y = 1)$, a Mach 10 shock wave is introduced to induce complex wave interactions within the fluid domain. This shock wave poses a significant challenge and provides insights into high-speed flow dynamics typical of supersonic conditions.

We performed computations on a grid of 960×240 using improved finite-volume WENO schemes of the third, fourth, fifth, and sixth orders, and obtained results at $t = 2$, as shown in Figure 2. It can be observed from the results that the fourth-order finite-volume WENO scheme exhibits superior analytical capabilities comparable to a sixth-order scheme on the same grid, particularly in resolving vorticity of flow and shock waves.

This test contrasts the performance of improved finite-volume WENO schemes of different orders in complex flow fields. Particularly on high-resolution grids, it demonstrates the outstanding numerical stability and analytical performance of the improved finite-volume WENO scheme, offering a more effective and reliable numerical simulation tool for solving complex wave systems and flow structures.

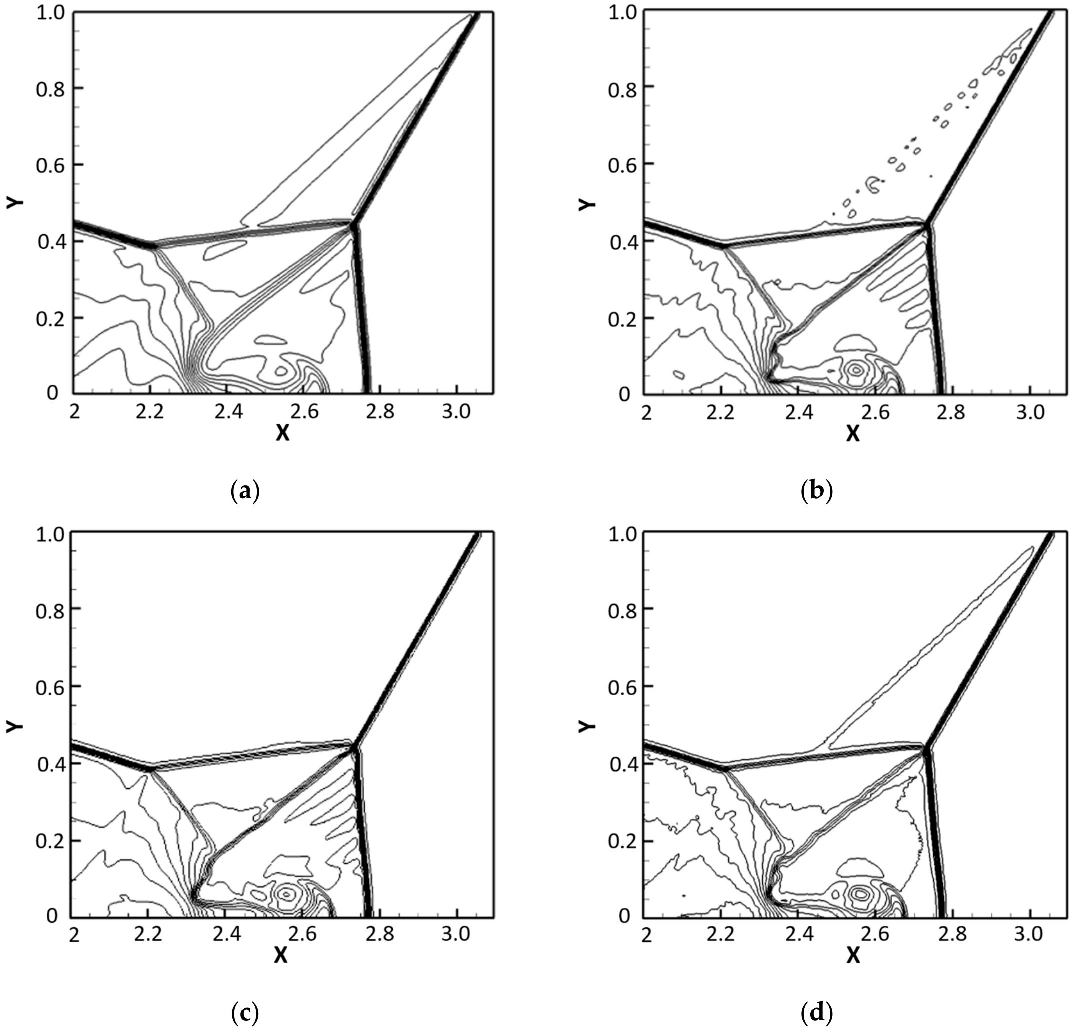

Figure 2. The flow fields of double shock wave reflections computed using different improved finite-volume schemes: (**a**) 3rd-order; (**b**) 4th-order; (**c**) 5th-order; (**d**) 6th-order.

3.3. Numerical Simulation of Rayleigh–Taylor Instability (RT Problem)

The Rayleigh–Taylor instability (RT problem) is a significant phenomenon in fluid dynamics that describes the instability and vortex formation when a shock wave interacts with an interface between two fluids of different densities. In this study, specific initial conditions were set within a computational domain of [0, 0.25] $\times$ [0, 1], and computations were performed using improved finite-volume WENO schemes. The initial conditions involve complex flow structures resulting from shock interactions between two fluids of different densities. The initial conditions are as follows:

$$(\varrho, u, v, p)^T = \begin{cases} (2, 0, -0.025c\cos(8\pi x), 1+2y)^T & 0 < y < 1/2, \\ (1, 0, -0.025c\cos(8\pi x), y+3/2)^T & x < 1, y < 1, \end{cases} \tag{10}$$

where $c = \sqrt{\frac{\gamma p}{\rho}}$ and $\gamma = \frac{5}{3}$.

The boundary conditions are set as follows:

- Left and right boundaries: anti-symmetric boundary conditions.
- Bottom boundary: $(\rho, u, v, p) = (2, 0, 0, 1)$.
- Top boundary: $(\rho, u, v, p) = (1, 0, 0, 2.5)$.

The computational domain grid size is 480 $\times$ 480, and the computed density contour plot is shown in Figure 3, with equally spaced contour levels ranging from 0.56 to 1.67.

Figure 3 compares the results obtained using the new WENO schemes of orders 4, 6, and 8 (referred to as WENO4, WENO6, and WENO8) with the results from the original WENO-ZQ (5th-order) scheme. Notably, the new WENO schemes demonstrate richer flow details, exhibiting larger vortex structures and well-developed smaller vortices compared to the WENOZQ results.

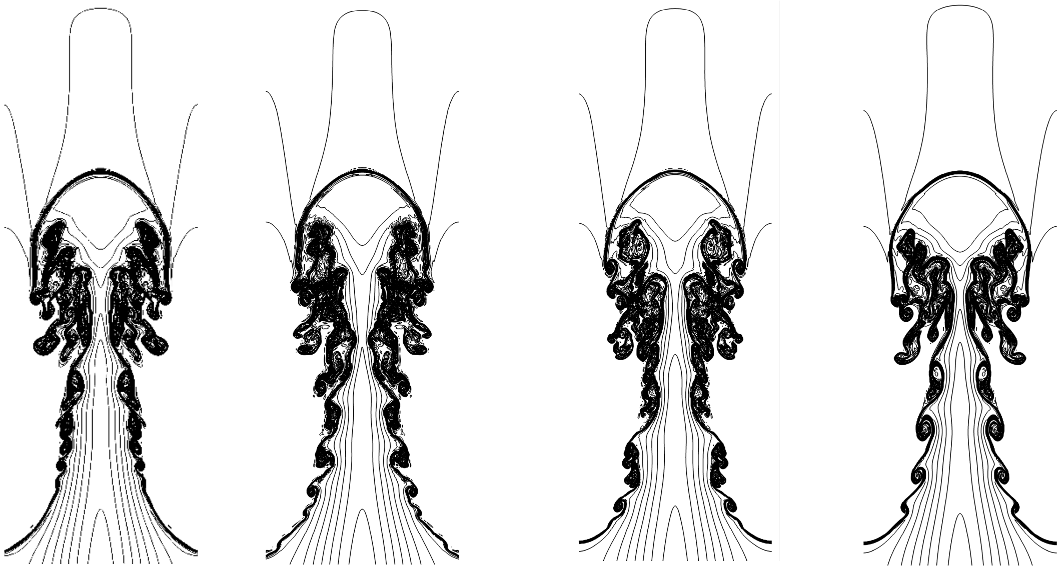

(**a**) (**b**) (**c**) (**d**)

Figure 3. Results of different numerical formats for solving RT problems. (**a**) WENO4; (**b**) WENO6; (**c**) WENO8; (**d**) WENO-ZQ.

4. Application Examples for Turbomachinery

4.1. RANS

In this section, Menter's shear stress transport (SST) two-equation $k - \omega$ turbulence model [26] is employed. To address flows ranging from essentially incompressible to supersonic Mach numbers, a preconditioning technique [27] is introduced into the time-derivative term of the compressible governing equations. The nonlinear system of equations is solved using Newton's implicit method, with symmetric Gauss–Seidel relaxation employed as a secondary method to solve the linear system of equations at each Newton iteration. This approach offers broad applicability, effectively tackling flow problems across various Mach numbers, while Newton's implicit method ensures the accurate modeling of nonlinear effects. WENO-ZQ3 and WENO-JS3 will be applied to reconstruct the interface conservative variables of convective flux.

4.1.1. NASA Stage 35

NASA Stage 35 is one of four inlet stages (Stages 35, 36, 37, 38) designed by NASA Glenn Research Center for an eight-stage core compressor with a pressure ratio of 20 in the 1970s, representing an advanced transonic core compressor. It is a low-aspect-ratio transonic axial-flow compressor. Its basic design parameters are shown in Table 1, and a detailed design description and test results can be found in references [28,29].

The wall of the grid is encrypted, and the minimum grid spacing is 1×10^{-6} m to ensure that the minimum grid spacing on the wall is $\Delta y^{+} < 1$. There are 73 nodes in the radial distribution of the grid, including 17 nodes at the gap, with a total grid count of 1.64 million. A grid diagram of the Stage 35 blade surface and middle section is shown in Figure 4. The wall and hub casing are set as no-slip boundary conditions, and the inlet and outlet parameters, as well as the rotor speed, are set according to Table 1.

Table 1. Main design parameters of Stage 35.

Parameters	Values
Rotor rpm at 100% speed	17,188.7 rpm
Rotor aspect ratio	1.19
Stator aspect ratio	1.26
Number of rotor blades	36
Number of stator blades	46
Mass flow rate	20.2 kg/s
Total pressure ratio	1.8

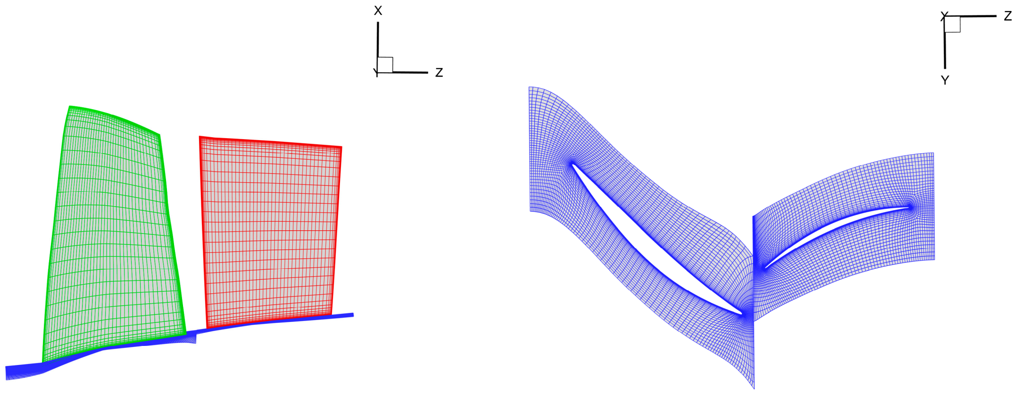

(**a**) (**b**)

Figure 4. Grid diagram of stage 35. (**a**) Blade surface; (**b**) middle section.

Figure 5 compares the calculation results of the Stage 35 characteristic lines with the test results. It can be seen that the calculation results using WENO-ZQ3 are in good agreement with the experimental results. However, due to the poor stability of WENO-JS3 in cases of large separation, the stall margin calculated differs significantly from the experimental results.

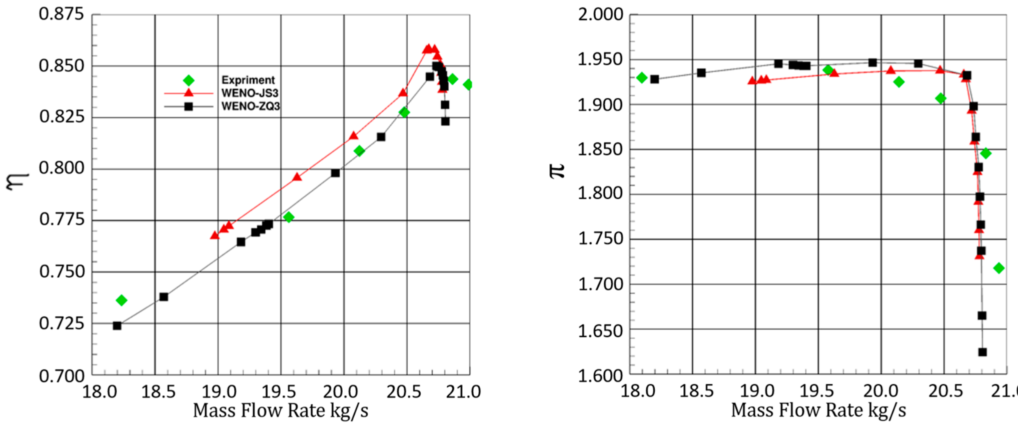

(**a**) (**b**)

Figure 5. Calculation results of stage 35 characteristic line. (**a**) Efficiency; (**b**) pressure ratio.

The surge phenomenon is involved in the simulation of the compressor, which is extremely unstable and difficult to predict. The results of WENO-ZQ3 are better than those of WENO-JS3 in stage 35. The aerodynamic flow field simulation of the turbine is simpler than that of the compressor, and the results of WENO-ZQ3 and WENO-JS3 are similar. WENO-ZQ3 is especially suitable for compressor simulation.

4.1.2. Pratt and Whitney Energy-Efficient Engine High-Pressure Turbine

The high-pressure turbine designed by Pratt and Whitney for the NASA Energy-Efficient Engine program (PW E3) is a single-stage turbine characterized by high load and high efficiency, and has 24 guide vanes and 54 rotor blades. The test [30,31] includes an uncooled rig program, a supersonic cascade rig program, and a leakage flow rig program. In this paper, Build 2 with a 43% reaction force in the uncooled rig program is utilized for verification. Specific data are shown in Table 2.

Table 2. Design-point test performance and status of uncooled rig program.

Parameters	Values
Total inlet temperature	431.17 K
Total inlet pressure	375.56 Kpa
Speed	9789 rpm
Total pressure ratio	4.12
Efficiency	90.8%
Correct rotor clearance	0.3683 mm

The wall of the grid is encrypted, and the minimum grid spacing is 1×10^{-6} m to ensure that the minimum grid spacing on the wall is $\Delta y^{+} < 1$. The total grid number of a single blade channel is approximately 2.27 million nodes. The grid distribution is shown in Figure 6. In order to ensure that the calculation results are independent of the grid distribution, steady calculations with different coarse and fine grids are used, demonstrating that 2.27 million nodes are sufficient for this study and can meet the required accuracy. The wall and hub casing are set as no-slip boundary conditions, and the inlet and outlet parameters, as well as the rotor speed, are set according to Table 2.

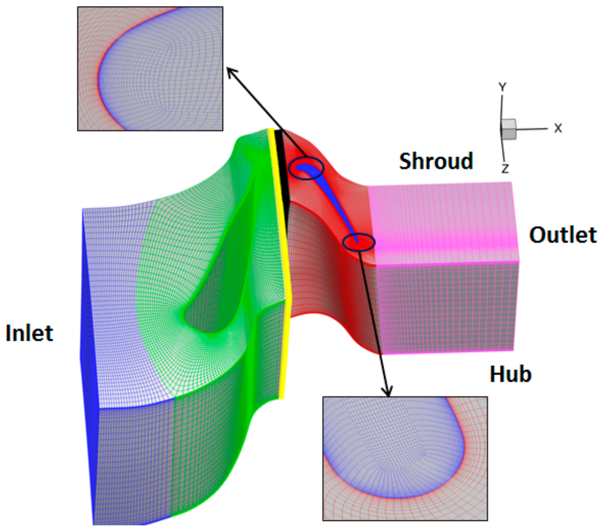

Figure 6. Computational grid of PW E3.

A comparison of the steady-state efficiency obtained in our experiments with that of the NASA experiments is shown in Figure 7. Compared with the experimental results, it is found that the design-point state prediction is better, the overall prediction efficiency is high, and the error is within 1%. Figure 8 shows a comparison of the static pressure distribution on the blade surface at the root, middle, and tip of the guide vane at the design point with WENO-ZQ3 and the experimental results. It can be seen that the static pressure distribution on the pressure surface in these three sections closely matches the experimental values, while the trailing edge of the blade-root suction surface shows slight differences.

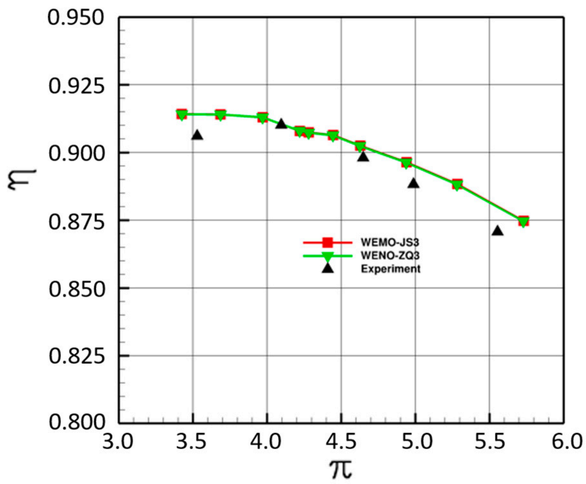

Figure 7. Mass-averaged efficiency vs. pressure ratio of PW E3.

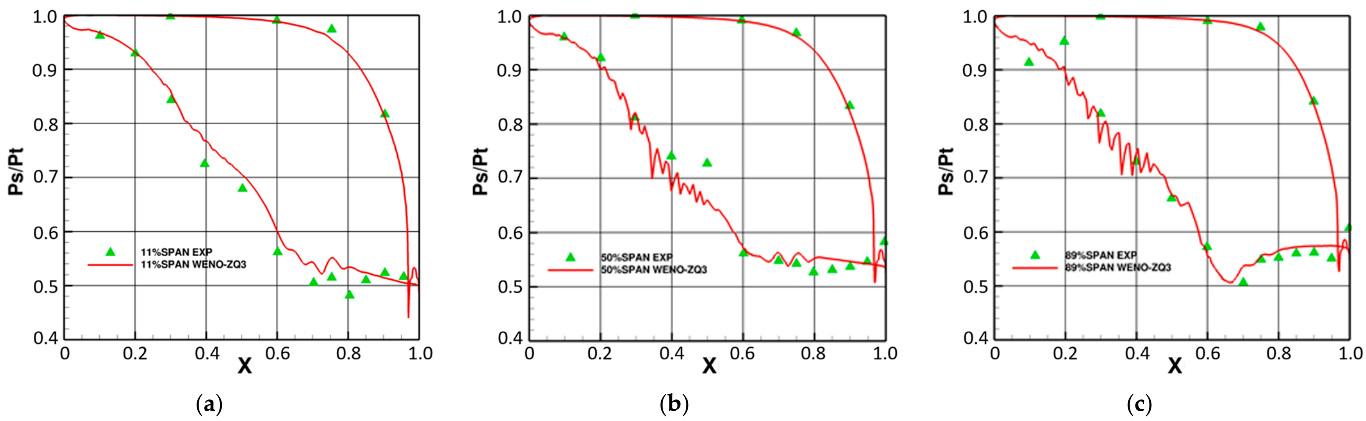

Figure 8. Pressure distribution of the guide vane: (**a**) 11% span; (**b**) 50% span; (**c**) 89% span.

4.2. Hybrid RANS/LES Model Menter SST-SAS

RANS-LES coupled simulations have recently been a hot topic in research. This is because this method not only saves a significant number of computational resources compared to LES and DNS, but also exhibits good analytical capabilities for large-scale structures in the mainstream flow [32]. Therefore, in 2018, Menter proposed a new coupling method known as the Scale-Adaptive Simulation (SAS) model [33]. This method constructs a source term in the ω-transport equation of the SST model, which is defined by a series of variables. Later, Wang [34] made revisions to the Karman length. The formulation of the SST-SAS model and the improved von Kármán scale L_{vk} are as follows:

$$Q_{\mathrm{SAS}} = \max\left[\rho\zeta_2\kappa S^2\left(\frac{L}{L_{\mathrm{vK}}}\right)^2 - C_{\mathrm{SAS}}\frac{2\rho k}{\sigma_\Phi}\max\left(\frac{|\nabla\omega|^2}{\omega^2},\frac{|\nabla k|^2}{k^2}\right),0\right], \tag{11}$$

$$\begin{gathered}
L_{\mathrm{vK}} = \max\left(\kappa\left|\frac{U'}{U''}\right|, C_S\sqrt{\frac{\kappa S_2}{(\beta/C_\mu)-\gamma}}\cdot\Delta\right),\\
\Delta = V_{\mathrm{CV}}^{1/3},\\
U' = C_1 S + C_2\Omega,\ S = \sqrt{2S_{ij}S_{ij}},\\
\Omega = \sqrt{2\Omega_{ij}\Omega_{ij}}, S_{ij} = \frac{(\partial U_i/\partial x_j)+(\partial U_j/\partial x_i)}{2},\\
\Omega_{ij} = \frac{(\partial U_i/\partial x_j)-(\partial U_j/\partial x_i)}{2}, U'' = \sqrt{\frac{\partial^2 U_i}{\partial x_k^2}\frac{\partial^2 U_i}{\partial x_j^2}}.
\end{gathered} \tag{12}$$

In Equation (11), $\varsigma_2 = 3.51, \kappa = 0.41, C_{SAS} = 2.0, \sigma_\Phi = 2/3$, L_{vK} represents the Kármán scale, and L represents the turbulence model scale. The Kármán scale is defined by Menter using a combination of the first and second derivatives of velocity. In the original Kármán scale, the first derivative of velocity is defined solely by the mean strain rate S. Wang, based on Helmholtz's velocity decomposition theorem, improved the first derivative of velocity to be defined by both the mean strain rate S and the mean vorticity. The tensor forms of strain rate and vorticity are provided in Equation (12).

SST-SAS turbulence model demonstrates excellent responsiveness to unsteady flows, effectively triggering LES mode in unsteady regions. The high-accuracy format determines the resolution of the flow field under LES mode given the presence of unsteady flow structures such as wakes and secondary flows in high-pressure turbine flow fields. In this summary, we focus on the wake, which is small and difficult to capture in the high-pressure turbine, and the results of WENO-ZQ5 are compared with those in the literature.

4.2.1. Numerical Calculation of LS89

Due to its extensive experimental data covering high- and transonic-flow conditions, LS89 serves as an ideal simulation target. In the present study, Figure 9 illustrates the computational domain grid for the case study, where the mesh is refined near the leading and trailing edges. The first-layer grid height is set to 0.0015 mm to ensure that $\Delta y^+ < 1$. Lin [35] used 20.46 million grids with WENO-JS5 in a Delayed Detached-Eddy Simulation (DDES), and E. Collado Morata adopted 29.7 million grids with a fourth-order centered scheme in Large Eddy Simulation. However, in this case, the total mesh cells are only 7 million with WENO-ZQ5, which are divided into 76 blocks for parallel computation. Tables 3 and 4, respectively provide the geometric data of the LS89 vane and details of two typical high-subsonic operating conditions.

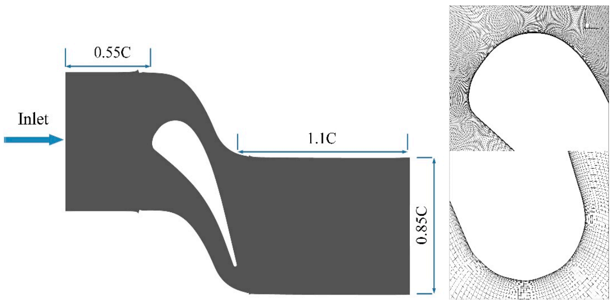

Figure 9. Computational domain and mesh of VKI LS89.

Table 3. Characteristic dimensions of VKI LS89.

Parameters	Values
Chord length (mm)	67.647
Axial chord length (mm)	36.985
Pitch-to-chord ratio (-)	0.850
Throat-to-chord ratio (-)	0.2207
Flow inlet angle (degree)	0
Stagger angle (degree)	55.0
Trailing-edge diameter (mm)	1.42

Table 4. Boundary conditions of VKI LS89.

Flow Conditions	$T^*_{inl}(K)$	$P^*_{inl}(Pa)$	$\alpha_{inl}(degree)$	$P_{out}(Pa)$	Ma_{ex}
MUR129	409.2	184,900	0	116,500	0.84
MUR235	413.3	182,800	0	104,900	0.927

The distribution of the entropy Mach number for the LS89 airfoil under the MUR129 condition is presented in Figure 10. This figure compares the results obtained in this study with the experimental and LES data, showing complete consistency. This indicates that the use of the high-order novel WENO format coupled with the SST-SAS model, as described in the text, achieves computational accuracy comparable to LES with fewer grid points. Additionally, a monitoring point is placed at the trailing edge to monitor pressure data and is represented by power spectral density (PSD) obtained using Fourier transform. The PSD curves in Figure 11 follow the $-5/3$ law, indicating that the inertial region of turbulence is correctly resolved by the present SAS. Moreover, the peak frequency of the trailing-edge shedding vortex is shown in the graph as 37.5 kHz, consistent with the shedding frequency of the reference [35]. The grid quantity, the turbulence model, and the numerical scheme adopted in the current case are feasible.

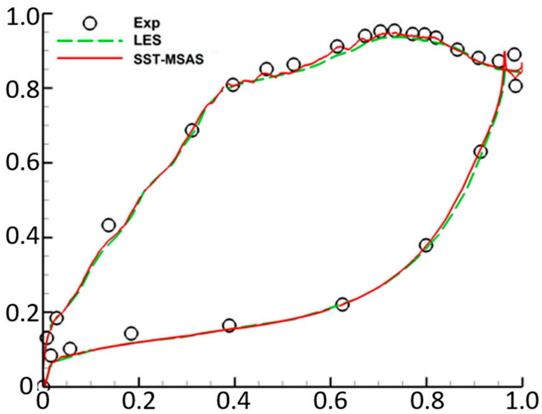

Figure 10. Isentropic Mach number distributions of flow condition MUR129.

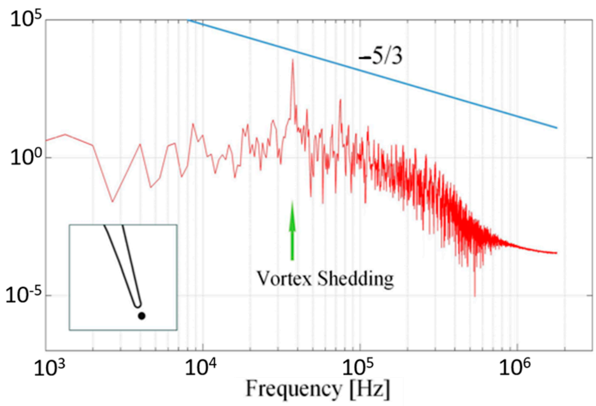

Figure 11. Power spectral density of the present SAS under flow condition MUR129.

According to the studies by Strelets [36] and Liu, Xiao, and Fu [37], excessive dissipation in the scheme strongly affects the simulation in the separation area, dampening small-scale coherent structures in the LES regions. Figure 12 demonstrates the dimensionless density gradient obtained for flow condition MUR235 from Table 4, comparing the results obtained using different WENO schemes with fifth-order accuracy. The WENO-JS scheme exhibits insufficient resolution in wake vortex aspects, indicating that the scale-resolving capability is not fully utilized. In contrast, the improved finite-volume WENO scheme offers higher accuracy in capturing shock waves, trailing-edge pressure waves, and their reflection waves, while also resolving more small-scale structures in the wake vortex system. Additionally, it is noteworthy that the computational time for the WENO-ZQ format is 10.53% less than that for the classical WENO-JS format, making it more cost-effective.

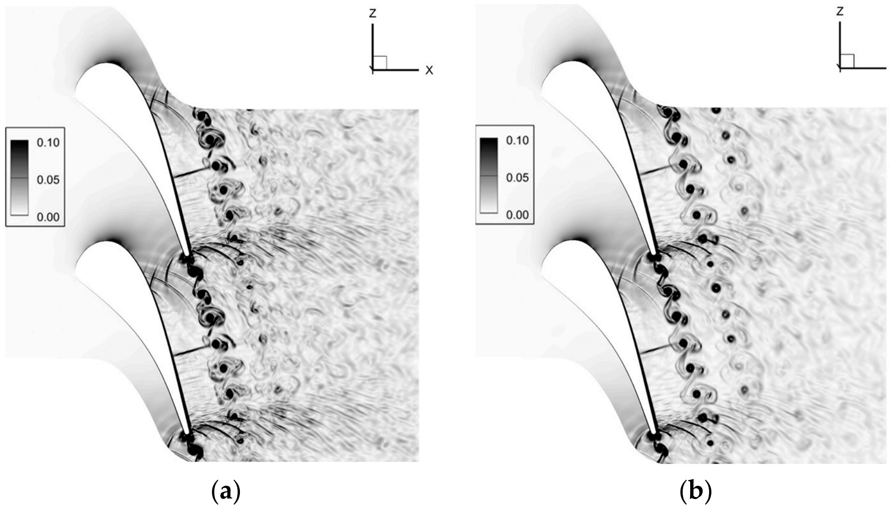

Figure 12. Comparison of numerical Schlieren calculation results under different WENO schemes. (**a**) WENO_ZQ; (**b**) WENO_JS.

4.2.2. Simulation of Film Cooling Based on C3X Cascade

The simulation of flat-plate film cooling on a turbine blade was compared with the experimental results obtained by Ames [38] in 1998 on C3X turbine blade film cooling. The experimental turbine blade operated at approximate chord-based Reynolds numbers of 800,000 and 500,000 at exit Mach numbers of about 0.27 and 0.17, respectively. And the coolant hole diameter was $D = 1.59$ mm. These Reynolds numbers fall within the relevant numerical range for medium-sized gas turbines. This study compared the experimental data for suction-side single-row holes. The turbine blade geometry data and computational setup parameters are detailed in Tables 5 and 6.

Table 5. Characteristic dimensions of C3X.

Parameters	Values
Chord length (mm)	144.93
Axial chord length (mm)	78.16
Pitch-to-chord ratio (-)	0.812
Throat-to-chord ratio (-)	0.227
Flow inlet angle (degree)	0
Stagger angle (degree)	55.47
Exit flow angle (degree)	72.4

Table 6. Boundary conditions of C3X cooling film.

Ma_{in}	$T^*_{inl}(K)$	$P^*_{inl}(Pa)$	Ma_{ex}	$P_{out}(Pa)$	$T_{cool}(K)$	VR	DR
0.0793	297.34	97262	0.2702	92451	317.39	0.49	0.94

The cascade computational domain adopts an HOH topology to ensure grid orthogonality, with a minimum grid spacing at the wall of 0.0015 mm. The first layer of the wall grids satisfies $\Delta y^+ < 1$. The total number of grids in a single airfoil passage is 6.5 million, with each individual film hole having 30,000 grids. The grid domain of the airfoil and film holes is depicted in Figure 13. The calculation employs the SST-MSAS turbulence model, and the fifth-order novel WENO-ZQ high-precision format reconstructs the interface conservation quantities. The RANS equations are solved using the implicit LU-SGS method. At the inlet boundary, the total temperature, total pressure, and inflow angle are specified. The outlet boundary is designed as a subsonic outflow boundary. The blade surface is modeled as a no-slip adiabatic boundary, while the film hole outlet participates directly in the flow field solution using area-weighted average interpolation. The film hole walls are modeled as no-slip adiabatic boundaries.

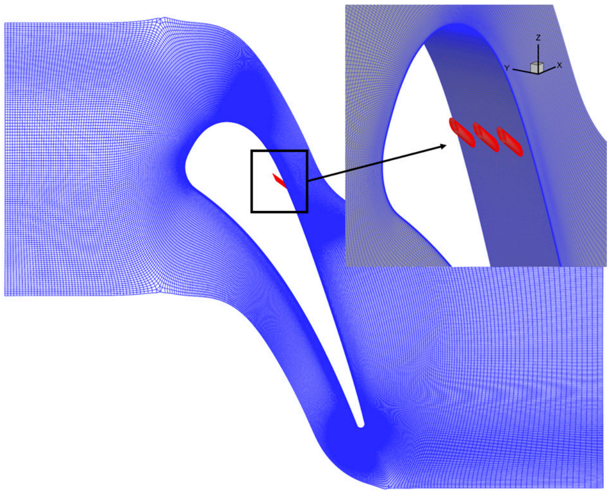

Figure 13. Film cooling computational domain of C3X cascade.

The prediction of cooling efficiency near film cooling holes has long been a challenge for scholars, due to the highly complex flow field generated by the continuous injection of jets into the mainstream. According to the jet mechanism reported in the relevant literature, the presence of jets resembles flow around a cylinder, forming a stagnation point at the jet's leading edge, thereby creating a horseshoe vortex around the leading edge. As the jet enters the mainstream, it forms kidney-shaped vortex pairs downstream of the hole. The momentum of the jet entering the mainstream determines the strength of these kidney-shaped vortex pairs, and excessive jet momentum can lead to the phenomenon of jet lifting near the hole. This series of complex flow phenomena renders the prediction of film cooling efficiency near the holes a challenging task.

This case study employs a fifth-order improved finite-volume WENO scheme, significantly enhancing the predictive accuracy of the simulation code. Figure 14 compares the calculated and experimental results of the centerline film cooling efficiency $\{\eta_{aw} = (T_{aw} - T_r)/(T_c - T_r)\}$ along the suction surface, where T_{aw} is the adiabatic wall temperature and T_r is the recovery temperature. It can be observed that the cooling efficiency decreases rapidly along the centerline and then levels off in downstream regions, showing good quantitative agreement with the experimental results. Figure 15 depicts contour plots of the average vorticity and average strain rate near the film cooling holes on the suction surface of the blade upon extracting flow fields near the film cooling holes. There is a noticeable increase in vorticity and strain rate along both sides beneath the film cooling holes, indicating the formation of kidney-shaped vortices as the jets entrain into the mainstream flow downstream, gradually mixing with the mainstream. In Figure 15a,b, high vorticity and strain rate occur near the leading edge of the jet. Combined with mechanistic analysis, this position corresponds to a stagnation point in the mainstream flow, where a horseshoe vortex forms. The range of existence of the horseshoe vortex coincides with the positions of high vorticity and strain rate near the leading edge in Figure 15. Thess phenomena are consistent with the trend of cooling effectiveness shown in Figure 14.

In summary, through the application of the fifth-order WENO-ZQ scheme, numerical calculations of film cooling can accurately describe flow field phenomena, and the accuracy of predicting film cooling efficiency is also guaranteed.

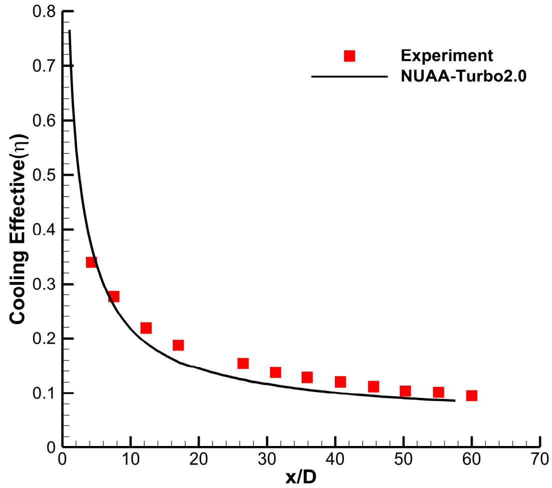

Figure 14. Centerline film cooling effectiveness of the suction surface in C3X cascade.

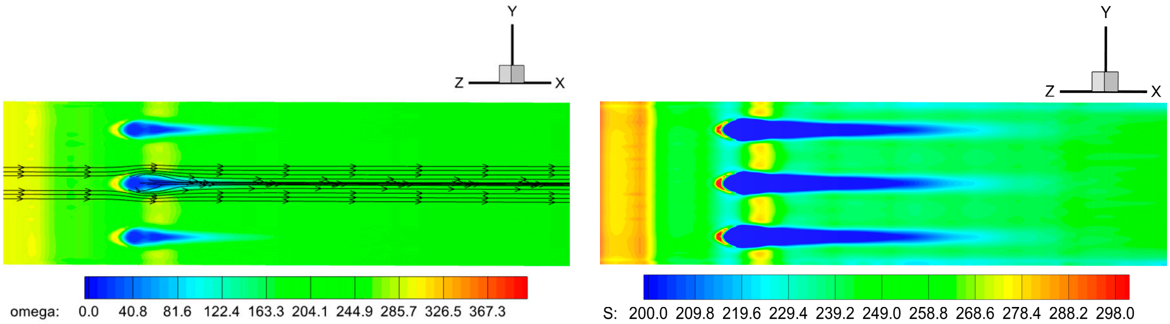

(**a**) (**b**)

Figure 15. Contour of average vorticity Ω and average strain rate S. (**a**) Mean vorticity Ω; (**b**) mean strain rate S.

5. Conclusions

Although many high-order WENO schemes have been developed in the field of computational fluid dynamics, most of them are challenging to apply in engineering. Either the calculation process is too complex for practical applications, or the calculations are highly unstable. However, WENO-ZQ overcomes the drawbacks of many WENO schemes by eliminating the need for computing linear weights, thereby enhancing computational stability. It not only reduces computational costs in aerodynamic applications by using fewer grid points, but also captures more fluid physics details.

This paper applies the finite-volume adapted WENO-ZQ scheme to simulate internal flows in aircraft engines, incorporating characteristic lines of turbomachinery and specific flow field details using the RANS and RANS/LES coupling methods. And typical turbine aerodynamic phenomena, including turbine wakes and film cooling, are also simulated. The results show that the third-order format of this scheme reduces the average error of the efficiency characteristic line calculation of the compressor from 0.76% to 0.05% compared to WENO-JS3, and the calculated turbine guide vane pressure distribution has an error of no more than 1% compared to the experimental value. In the high-precision numerical calculations of film cooling, the error of the centerline distribution of film cooling efficiency with the experimental value does not exceed 3%. Therefore, WENO-ZQ is a rare high-precision numerical calculation method with low computational cost, good robustness, and easy implementation in engineering software applications.

Author Contributions: Conceptualization, H.W. and S.Z.; methodology, H.W. and S.Z.; software, D.Z.; validation, H.W. and D.Z.; formal analysis, H.W.; investigation, H.W.; resources, N.G.; data curation, X.W.; writing—original draft preparation, H.W.; writing—review and editing, H.W.; visualization, X.W.; supervision, N.G.; project administration, N.G.; funding acquisition, X.W. All authors have read and agreed to the published version of the manuscript.

Funding: This research was funded by National Science and Technology, grant number Y2019-I-0018-0017.

Institutional Review Board Statement: Not applicable.

Informed Consent Statement: Not applicable.

Data Availability Statement: The original contributions presented in the study are included in the article, further inquiries can be directed to the corresponding author.

Conflicts of Interest: The authors declare no conflicts of interest.

References

1. Harten, A.; Engquist, B.; Osher, S.; Chakravarthy, S.R. Uniformly high order accurate essentially non-oscillatory schemes, iii. *J. Comput. Phys.* **1987**, *71*, 231–303. [CrossRef]
2. Zhong, D.; Sheng, C. A new method towards high-order weno schemes on structured and unstructured grids. *Comput. Fluids* **2020**, *200*, 104453. [CrossRef]
3. Liu, H.; Qiu, J. Finite difference hermite weno schemes for hyperbolic conservation laws. *J. Sci. Comput.* **2015**, *63*, 548–572. [CrossRef]
4. Balsara, D.S.; Garain, S.; Florinski, V.; Boscheri, W. An efficient class of WENO schemes with adaptive order for unstructured meshes. *J. Comput. Phys.* **2020**, *404*, 109062. [CrossRef]
5. Liu, X.D.; Osher, S.; Chan, T. Weighted essentially non-oscillatory schemes. *J. Comput. Phys.* **1994**, *115*, 200–212. [CrossRef]
6. Jiang, G.S.; Shu, C.W. Efficient implementation of weighted ENO schemes. *J. Comput. Phys.* **1996**, *126*, 202–228. [CrossRef]
7. Hu, C.; Shu, C.W. Weighted essentially non-oscillatory schemes on triangular meshes. *J. Comput. Phys.* **1999**, *150*, 97–127. [CrossRef]
8. Shi, J.; Hu, C.; Shu, C.W. A technique of treating negative weights in weno schemes. *J. Comput. Phys.* **2002**, *175*, 108–127. [CrossRef]
9. Friedrich, O. Weighted essentially non-oscillatory schemes for the interpolation of mean values on unstructured grids. *J. Comput. Phys.* **1998**, *144*, 194–212. [CrossRef]
10. Zhu, J.; Qiu, J. *Academic Lecture on High Order Accuracy Numerical Methods: A Simple and Efficient Finite Volume Weno Method*; Nanjing University of Aeronautics and Astronautics: Nanjing, China, 2020.
11. Zhu, J.; Qiu, J. A new fifth order finite difference weno scheme for solving hyperbolic conservation laws. *J. Comput. Phys.* **2016**, *318*, 110–121. [CrossRef]
12. Zhu, J.; Qiu, J. A new type of finite volume weno schemes for hyperbolic conservation laws. *J. Sci. Comput.* **2017**, *73*, 1338–1359. [CrossRef]
13. Zhu, J.; Shu, C.-W. Numerical study on the convergence to steady state solutions of a new class of high order weno schemes. *J. Comput. Phys.* **2017**, *349*, 80–96. [CrossRef]
14. Sheng, C.; Zhao, Q.; Zhong, D.; Ge, N. A strategy to implement high-order weno schemes on unstructured grids. In Proceedings of the AIAA Aviation 2019 Forum, Dallas, TX, USA, 17–21 June 2019; p. 2955.
15. Sheng, C.; Zhao, Q.; Baugher, S. Numerical investigation of rotor aerodynamics using high-order unstructured grid schemes. In Proceedings of the AIAA Scitech 2020 Forum, Orlando, FL, USA, 6–10 January 2020; p. 0528.
16. Sheng, C. Improving predictions of transitional and separated flows using rans modeling. *Aerosp. Sci. Technol.* **2020**, *106*, 106067. [CrossRef]
17. Balsara, D.S.; Garain, S.; Shu, C.-W. An efficient class of weno schemes with adaptive order. *J. Comput. Phys.* **2016**, *326*, 780–804. [CrossRef]
18. Zhao, Z.; Zhu, J.; Chen, Y.; Qiu, J. A new hybrid weno scheme for hyperbolic conservation laws. *Comput. Fluids* **2019**, *179*, 422–436. [CrossRef]
19. Zhu, J.; Qiu, J. A new type of modified weno schemes for solving hyperbolic conservation laws. *SIAM J. Sci.Comput.* **2017**, *39*, A1089–A1113. [CrossRef]
20. Lin, J.; Abgrall, R.; Qiu, J. High order residual distribution for steady state problems for hyperbolic conservation laws. *J. Sci. Comput.* **2019**, *79*, 891–913. [CrossRef]
21. Ji, Z.; Liang, T.; Fu, L. A class of new high-order finite-volume TENO schemes for hyperbolic conservation laws with unstructured meshes. *J. Sci. Comput.* **2022**, *92*, 61. [CrossRef]
22. De Vanna, F.; Avanzi, F.; Cogo, M.; Sandrin, S.; Bettencourt, M.; Picano, F.; Benini, E. URANOS: A GPU accelerated Navier-Stokes solver for compressible wall-bounded flows. *Comput. Phys. Commun.* **2023**, *287*, 108717. [CrossRef]
23. Roe, P.L. Approximate riemann solvers, parameter vectors, and difference schemes. *J. Comput. Phys.* **1981**, *43*, 357–372. [CrossRef]

24. Liou, M.S. A sequel to ausm, part ii: Ausm-up for all speeds. *J. Comput. Phys.* **2006**, *214*, 137–170. [CrossRef]
25. Shu, C.-W. *Essentially Non-Oscillatory and Weighted Essentially Non-Oscillatory Schemes for Hyperbolic Conservation Laws*; Springer: Berlin/Heidelberg, Germany, 2007; pp. 325–432.
26. Menter, F.R. Two-equation eddy-viscosity turbulence models for engineering applications. *AIAA J.* **1994**, *32*, 1598–1605. [CrossRef]
27. Sheng, C. A preconditioned method for rotating flows at arbitrary Mach number. *Model. Simul. Eng.* **2011**, *2011*, 29. [CrossRef]
28. Moore, R.; Reid, L. *Performance of Single-Stage Axial-Flow Transonic Compressor with Rotor and Stator Aspect Ratios of 1.63 and 1.78, Respectively, and with Design Pressure Ratio of 1.82*; NASA Technical Paper; Natbonal Aeronautics and Space Admtnislration: Washington, DC, USA, 1982.
29. Reid, L.; Moore, R.D. *Design and Overall Performance of four Highly Loaded, High Speed Inlet Stages for an Advanced High-Pressure-Ratio Core Compressor*; No. NASA-TP-1337, Natbonal Aeronautics and Space Admtnislration: Washington, DC, USA, 1978.
30. Gardner, W.B. *Energy Efficient Engine: High Pressure Turbine Uncooled Rig Technology Report*; No. NASA-CR-165149; Natbonal Aeronautics and Space Admtnislration: Washington, DC, USA, 1979.
31. Thulin, R.D.; Howe, D.C.; Singer, I.D. *Energy Efficient Engine High-Pressure Turbine Detailed Design Report*; No. NASA-CR-165608; Natbonal Aeronautics and Space Admtnislration: Washington, DC, USA, 1982.
32. Spalart, P.R. Strategies for turbulence modelling and simulations. *Int. J. Heat Fluid Flow* **2000**, *21*, 252–263. [CrossRef]
33. Egorov, Y.; Menter, F. Development and application of SST-SAS turbulence model in the DESIDER project. In *Advances in Hybrid RANS-LES Modelling, Proceedings of the 2007 Symposium of Hybrid RANS-LES Methods, Corfu, Greece, 17–18 June 2007*; Springer: Berlin/Heidelberg, Germany, 2008; pp. 261–270.
34. Wang, G.; Ge, N.; Zhong, D. Numerical investigation of the wake vortex-related flow mechanisms in transonic turbines. *Int. J. Aerosp. Eng.* **2020**, *2020*, 1–18. [CrossRef]
35. Lin, D.; Yuan, X.; Su, X. Local entropy generation in compressible flow through a high-pressure turbine with delayed detached eddy simulation. *Entropy* **2017**, *19*, 29. [CrossRef]
36. Strelets, M. Detached eddy simulation of massively separated flows. In Proceedings of the 39th AIAA Fluid Dynamics Conference and Exhibit, Reno, NV, USA, 8–11 January 2001; pp. 1–18.
37. Liu, J.; Xiao, Z.; Fu, S. Unsteady Flow Around Two Tandem Cylinders Using Advanced Turbulence Modeling Method. In *Computational Fluid Dynamics 2010, Proceedings of the Sixth International Conference on Computational Fluid Dynamics, ICCFD6, St. Petersburg, Russia, 12–16 July 2010*; Springer: Berlin/Heidelberg, Germany, 2011; pp. 879–881.
38. Ames, F.E. Aspects of vane film cooling with high turbulence: Part I—Heat transfer. *J. Turbomach.* **1998**, *120*, 768–776. [CrossRef]